Proton-Assisted Recoupling (PAR) in Peptides and Proteins

Citation: Donovan, Kevin J. et al. "Proton-Assisted Recoupling (PAR) in Peptides and Proteins." The Journal of Physical Chemistry B 121, 48 (November 2017): 10804–10817 © 2017 American Chemical Society

As Published: http://dx.doi.org/10.1021/acs.jpcb.7b08934

Publisher: American Chemical Society (ACS)

Persistent URL: http://hdl.handle.net/1721.1/118881

Version: Author's final manuscript: final author's manuscript post peer review, without publisher's formatting or copy editing

Rev1_171016

Proton Assisted Recoupling (PAR) in Peptides and Proteins

Kevin J. Donovan[†‡], Sheetal K. Jain[†‡], Robert Silvers[†], Sara Linse[§] and Robert G. Griffin[†*]

† Francis Bitter Magnet Laboratory and Dept of Chemistry

Massachusetts Institute of Technology

Cambridge, MA 02139

USA

§ Department of Biochemistry and Structural Biology

Lund University

SE22100 Lund, Sweden

‡ KJD and SKJ contributed equally to this work.

* rgg@mit.edu

Abstract

Proton assisted recoupling (PAR) is examined by exploring optimal experimental conditions and magnetization transfer rates in a variety of biologically relevant nuclear spin-systems including simple amino acids, model peptides and two proteins – nanocrystalline protein G (GB1), and importantly amyloid beta 1-42 ($M_0A\beta_{1\text{-}42}$) fibrils. A selective PAR protocol, SUBPAR (**S**etting **U**p **B**etter **P**roton **A**ssisted **R**ecoupling), is described to observe magnetization transfer in one-dimensional spectra, which minimizes experiment time (in comparison to 2D experiments) and thereby enables an efficient assessment of optimal PAR conditions for a desired magnetization transfer. In the case of the peptide spin systems, experimental and simulated PAR data sets are compared on a semi-quantitative level, thereby elucidating the interactions influencing PAR magnetization transfer, and their manifestations in different spin transfer networks. Using the optimum Rabi frequencies determined by SUBPAR, PAR magnetization transfer trajectories (or buildup curves) were recorded, and compared to simulated results for short peptides. PAR buildup curves were also recorded for $M_0A\beta_{1\text{-}42}$, and examined conjointly with a recent structural model. The majority of salient cross peak intensities observed in the $M_0A\beta_{1\text{-}42}$ PAR spectra are well modeled with a simple bi-exponential equation although the fitting parameters do not show any strong correlation to internuclear distances. Nevertheless, these parameters provide a wealth of invaluable semi-quantitative structural constraints for the $M_0A\beta_{1\text{-}42}$. The results presented here offer a complete protocol for recording PAR ^{13}C-^{13}C correlation spectra with high-efficiency, and using the resulting information in protein structural studies.

Introduction

Over the past decade magic angle spinning (MAS) NMR has made huge strides in methodology, sample preparation and instrumentation, so that it is now possible to obtain atomic level structures of proteins in large macromolecular assemblies not accessible by other techniques.[1-11] Determination of these structures requires measurement of multiple distance restraints from cross peak intensities in MAS spectra, and this requirement has stimulated the development of an extensive repertoire of dipolar recoupling experiments aimed at providing accurate distances and torsion angles.[12-26] Among the possible approaches for dipole recouping, proton assisted recoupling (PAR) has emerged as an extraordinarily promising technique for observing long-distance homonuclear correlations in MAS spectra at moderate-to-high spinning frequencies and high magnetic fields.[4, 27-31] For example, ^{13}C-^{13}C PAR correlation spectra were recently used to investigate a variety of Aβ fibril samples,[6, 7, 32] and provided over 500 distance restraints that were essential for resonance assignments and intra- and intermolecular structure determination.

The PAR mechanism utilizes *third spin assisted recoupling* (TSAR), which facilitates homonuclear magnetization transfer via a mutually coupled proton spin bath. Thus, PAR is a second-order recoupling technique, making it relatively immune to dipolar truncation, a phenomenon that attenuates weak, but structurally important long-range correlations in the presence of stronger, short-range correlations.[33] Specifically, PAR enables observation of long-distance cross peaks that either would not be present or would be weak when first order recoupling sequences are used, and it is these long-distance cross peaks that typically provide the most important distance constraints in protein structure calculations. Naturally, these observations invite the development of quantitative capabilities for PAR since there is currently no widely used, robust technique for accurately measuring homonuclear distances in protein samples with uniform isotopic labeling. In particular, while PAR spectra have previously been interpreted qualitatively, the PAR magnetization transfer process has not been assessed for quantitatively measuring internuclear distances.[27] These questions are in part stimulated by a recent paper in which *proton driven* *spin diffusion* (PDSD),[34, 35] an analogous but functionally different homonuclear recoupling technique, was used to simulate magnetization transfer curves and measure to high accuracy internuclear distances in tri-peptide systems.[36]

The PAR pulse sequence is comparatively simple, and is identical in form to cross polarization (CP).[37, 38] Nevertheless, recording high quality PAR data is often challenging, because the amplitudes of the simultaneous ^{1}H and ^{13}C continuous wave (CW) irradiation during PAR (i.e. Rabi frequencies) are critically important to achieve optimal magnetization transfer. Furthermore, in contrast to CP the optimum PAR transfer conditions are not determined by a simple analytical solution (i.e. the Hartmann-Hahn condition) but must be derived empirically. Earlier papers relied heavily on simulated PAR optimizations[27, 29, 30] of simplified spin systems and were not rigorously compared to experimental data. These simulations mostly indicated optimal PAR Rabi frequencies close to the static Hartmann-Hahn condition, with a slight mismatch (i.e. $\omega_{1H} \approx \omega_{13C}$) and with CW amplitudes exceeding the spinning frequency by a factor of 2 or more (i.e. $\omega_{1H}, \omega_{13C} \geq 2\omega_r$). In this publication we present a protocol for experimental PAR optimization, *Setting Up Better Proton Assisted Recoupling* (SUBPAR), that generates data for direct comparison to simulated polarization transfer plots. A systematic evaluation of magnetization transfer in a variety of compounds with SUBPAR shows a wide variation due to the presence of different local proton networks. This implies that every spin transfer pathway has a unique optimization landscape, which serves as a fingerprint of the local nuclear geometry. Some spin transfer pathways indicated optimum PAR transfer conditions close to the static Hartmann-Hahn condition while others showed optimal conditions with significantly mismatched values of ω_{1C} and ω_{1H}. A comparison of simulated PAR optimizations with variable parameters indicates which interactions are most influential in PAR magnetization transfer. For some of the spin systems we examined, a comparison of experimental and simulated PAR optimizations showed improved agreement as more spins are included in the simulations. However, for other spin systems, the simulated optimization trajectories converge with a limited number of spins (as few as 7) but with minimal, if any agreement to experimental data. This suggests that a more elaborate mathematical framework (to account for relaxation and other stochastic processes) combined with increased computational power is required to obtain a thorough, rigorous prediction of PAR magnetization transfer.

Second, this study explores the possibility of extracting quantitative dipole coupling information from PAR magnetization transfer trajectories (i.e. buildup curves). Detailed PAR buildup curves were recorded for glycine (Gly) and for the two selectively labeled tri-peptides alanyl-glycyl-glycine, AGG2 and AGG3, with two and three ^{13}C labels, respectively.[33, 36, 39] This enabled observation of magnetization transfer between specific spin pairs of known distance for direct comparison with corresponding simulations. Much like the comparison between experimental and simulated PAR optimizations, the experimental and simulated PAR buildups show similarity, but not a sufficiently close match to allow for extracting quantitative dipolar coupling parameters with numerical fitting procedures. However, this data offers an additional empirical calibration and provides further insight into the relative importance of the different interactions affecting PAR magnetization transfer.

Lastly, and perhaps most importantly, we describe a procedure for optimizing and analyzing PAR magnetization transfer data from protein samples. Extensive PAR optimizations are shown for the crystalline B1 immunoglobulin binding domain of protein G (GB1), and an amyloid beta 1-42 ($M_0A\beta_{1\text{-}42}$) fibril sample. Magnetization transfer rates (at a variety of different PAR conditions) are examined for many of the internuclear contacts that are most influential for structural calculations in $M_0A\beta_{1\text{-}42}$. These rates are analyzed with a structural model, providing a catalog of information for qualitative analysis. Thus, with the information provided here, PAR will provide an efficient and valuable approach for structural studies in a variety of amyloid and membrane protein systems of unknown structure.[10, 40-42] Furthermore, while this analysis currently offers a valuable quantitative application of PAR, it also provides the motivation for further quantitative investigations of PAR magnetization transfer, and the development of PAR-inspired techniques for increasingly precise internuclear distance measurements in MAS protein experiments.

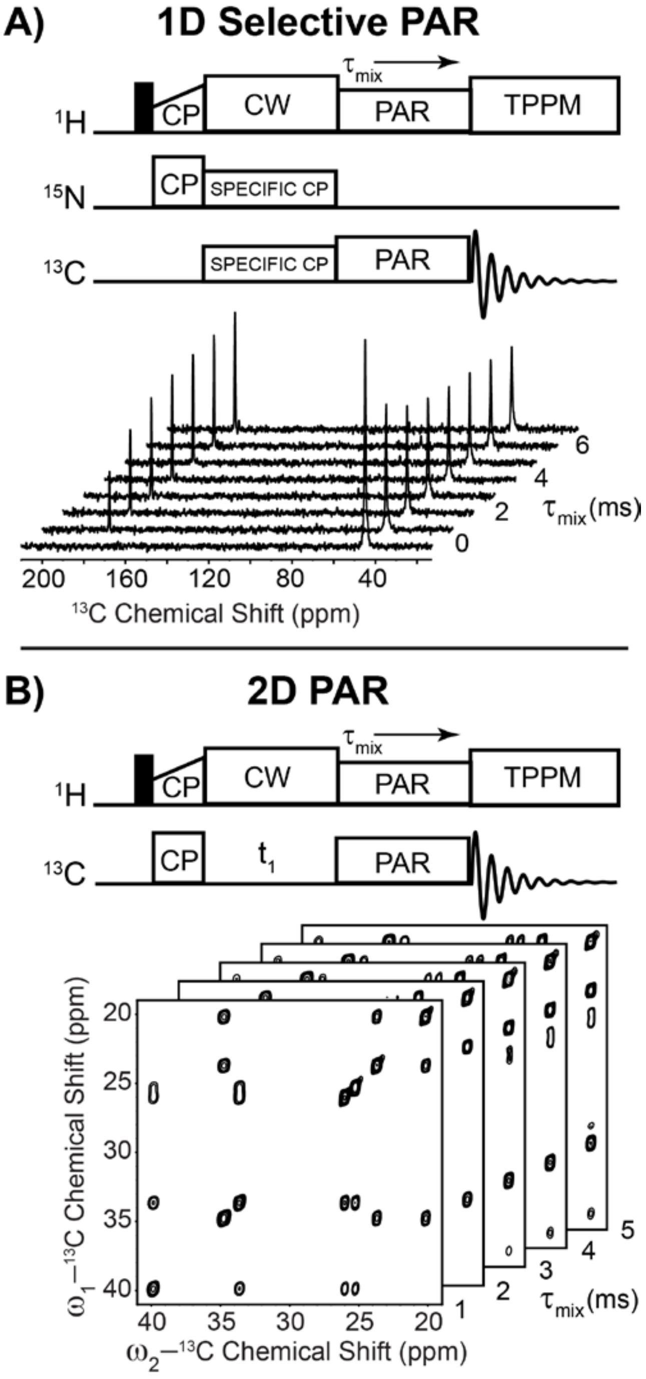

Figure 1. (A) PAR pulse sequences used to collect the data presented in this report. The 1D selective PAR sequence provides a faster experimental protocol for scanning the available ω_{rf}^C, ω_{rf}^H values to find the optimum conditions with SUBPAR. (B) The 2D sequence, while far more time-consuming, is the most robust protocol for observing PAR magnetization transfer between a specific spin pair and also provides more spectral dispersion to resolve peaks which overlap in a 1D spectrum.

Materials and Methods

Figure 1 illustrates the selective PAR protocol, which was first described by Lewandowski, et al.[30] The ^{1}H magnetization is transferred to the ^{15}N nuclei in the first CP period and then selectively from the ^{15}N nuclei either to the neighboring alpha (^{13}Cα) or carbonyl (^{13}CO) nuclei using the SPECIFIC-CP protocol.[43, 44] SPECIFIC-CP is used in order to observe the magnetization buildup on ^{13}C's that do not carry magnetization initially. Following the initial selective excitation, the PAR mixing period commences with CW irradiation (spin-lock) on both the ^{1}H and ^{13}C channels to drive magnetization transfer from the selected ^{13}C nuclei to all other ^{13}C nuclei. This pulse sequence allows for high-throughput scanning of PAR matching conditions (for SUBPAR optimization) and rapid acquisition of PAR buildup curves as the magnetization transfer can be observed in a single dimension and does not require incremented sampling of an indirect dimension as in 2D experiments.

The 2D polarization transfer plots shown in the following sections are the result of SUBPAR optimization procedures, and were recorded and processed using programmed macros to perform a grid search over the available range of PAR field intensities. The benefits of macro-driven automation are considerable, as constructing a 2D PAR polarization transfer plot requires the collection and analysis of approximately 1,000 different 1D data sets depending on the sampling increment, which if performed manually would be impractical and highly inefficient, if not altogether unfeasible.

Experimental

All experiments were performed on an Bruker Avance III 800 MHz spectrometer with samples packed in 3.2 mm rotors, and spinning at $\omega_r/2\pi$=20 kHz . The 10% ^{13}C, ^{15}N enriched samples (Gly, N-Ac-VL, AGG2 and AGG3) were prepared by mixing, dissolving and recrystallizing corresponding amounts of uniformly ^{13}C, ^{15}N enriched and natural abundance substrates. The GB1 sample was prepared following a previously published protocol,[2] and preparation details for the $M_0A\beta_{1\text{-}42}$ sample are published elsewhere.[6, 45]

The 2D pulse sequence shown in **Figure 1B** was used to collect the PAR buildup curves for AGG2, AGG3 and $M_0A\beta_{1-42}$, as the 1D protocol doesn't allow simultaneous acquisition of buildups for multiple site-specific polarization transfers. All 2D spectra contributing to the same buildup curves were collected in parallel by interleaving scans corresponding to different mixing times, so that any hardware fluctuations would have an equally weighted impact on all the data points in the build-up curve.

Simulations were performed with SIMPSON[46, 47] and simulated spin systems were created from Protein Data Bank (PDB) files using SIMMOL.[48] The effects of increased crystallite averaging were found to converge above 256 (α, β) orientations with 12 γ orientations, and hence these parameters were used for all simulations. The SIMPSON script used to generate the 2D polarization transfer plot for Gly (shown in Figure 2) is provided as an example in the Supporting Information (SI1).

Results and Discussion

I. SUBPAR Optimizations and Simulations in Model Systems

a. Rabi Frequency Optimization in Glycine

Glycine, displaying two well-separated isotropic ^{13}C chemical shifts, was chosen as the initial model compound for this study as it is the simplest biologically relevant spin system for investigating ^{13}C-^{13}C magnetization transfer. **Figure 2** compares an experimental PAR polarization transfer plot obtained using the SUBPAR protocol described in the previous section with a corresponding simulation measuring PAR polarization transfer from I_{1x} (initial, transverse magnetization on ^{13}Cα) to I_{2+} (observable magnetization on carbonyl nucleus) after τ_{mix}=3 ms. The sample was prepared with 10% ^{13}C,^{15}N enrichment (see Materials and Methods) to ensure that only intramolecular polarization transfer was observed. The spin system simulated for Gly was constructed from the previously published crystal structure.[49] Optimum PAR transfer in the Gly spin system was found to occur experimentally with $\omega_{1C}/2\pi =$ 72 kHz and $\omega_{1H}/2\pi =$ 81 kHz, and with $\omega_{1C}/2\pi =$78.5 kHz and $\omega_{1H}/2\pi =$ 74 kHz in the simulations. The top 5, 10, and 20 PAR polarization transfer conditions for the experimental and simulated data shown in **Table 1** were all found to occur in approximately the same region of the 2D polarization transfer plot (70-83 kHz on both channels). The fifth highest condition generated approximately 97% of the magnetization transfer produced by the Rabi frequencies, and thus would still be an excellent choice for PAR experiments.

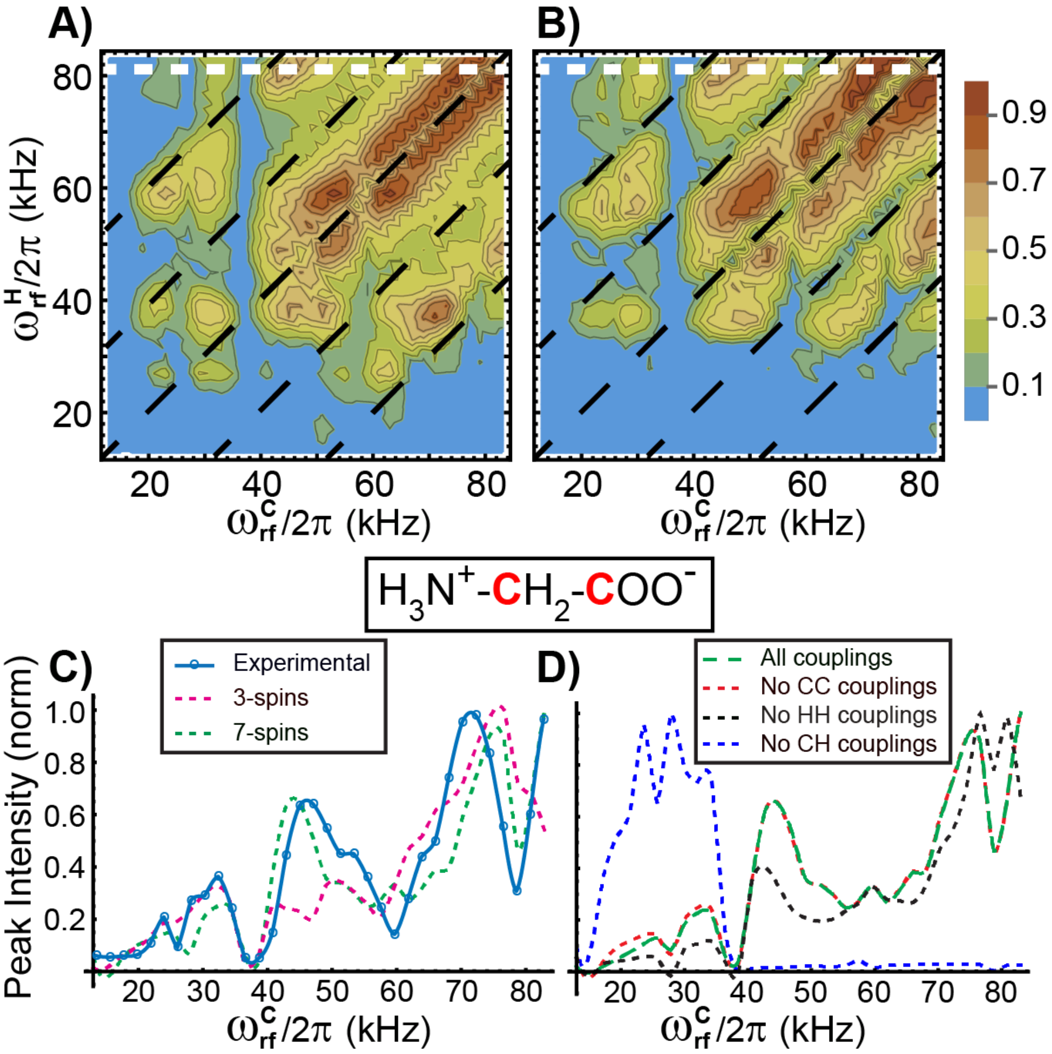

Figure 2. Experimental (A) and simulated (B) SUBPAR optimizations for Gly. The diagonal black dashed lines in the 2D RF optimization plots shown in (A) and (B) indicate CP conditions (n=0,±1,±2), and the horizontal white dashed lines show the position of the 1D traces displayed in (C) and (D). Both 2D and 1D data sets were normalized to their maximum intensities. The 1D traces (corresponding to $\omega_{rf}^{H}/2\pi$ = 80.9 kHz) shown in (C) illustrate the increasing agreement between experimental and simulated data as the simulated spin system is expanded to include more spins from the molecular structure. The simulated traces shown in (D) were acquired by selectively excluding the given dipole coupling interactions, indicating that the most influential is the ^{1}H-^{13}C dipole coupling and the least influential is ^{13}C-^{13}C dipole coupling, which has virtually no impact on the calculated RF trajectory.

Figure 2 displays a noticeable agreement between the experimental and simulated data that is fully appreciated by comparing 1D traces extracted from the 2D plots (as shown in **Figure 2C**), corresponding to a 1D sweep of the ^{13}C Rabi frequency, at constant ^{1}H RF field strength. The 1D traces illustrate the increasing agreement between experimental and simulated data as the size of the simulated spin system is increased to include more ^{1}H's. The closest agreement to the experimental data was achieved with the largest simulated spin system that contained both ^{13}C nuclei and all of the ^{1}H's in the Gly zwitterion. The trend of increasing agreement between simulated and experimental data as additional ^{1}H nuclei are included in the simulated spin system suggests that all of the Gly ^{1}H's play a significant role during PAR magnetization transfer from the ^{13}Cα to the ^{13}CO. Furthermore, this trend suggests that incorporating ^{1}H nuclei from neighboring molecules in the unit cell into the simulated spin system may further improve the agreement between experimental and simulated data. The longest 1D simulation shown in **Figure 2C** (which used 7 spins) required approximately 39 minutes on a 2.2 GHz quad core processor.

Table 1. Optimum PAR conditions from SUBPAR optimizations shown in **Figure 1**. Percent transfer is shown normalized to the optimum condition to reflect the relative efficiencies of the different RF field values.

	$\omega_{1C}/2\pi, \quad \omega_{1H}/2\pi\,(kHz)$		**Percent Optimal Transfer**	
PAR Condition	**Experiment**	**Simulation**	**Experiment**	**Simulation**
1	72.4, 80.9	78.5, 74.0	100	100
2	70.3, 78.8	80.7, 83.0	99.9	99.4
3	83, 80.9	80.7, 76.2	98.4	98.8
4	70.3, 80.9	78.5, 80.7	97.2	98.4
5	80.9, 78.8	74, 69.5	97.1	96.2
10	83, 78.8	67.2, 62.7	94.6	93.8
20	72.4, 70.3	58.2, 60.4	87.2	88.0

Figure 2D illustrates the role of different dipole coupling categories on the simulated 1D ^{13}C polarization transfer profiles. Each 1D simulated profile was acquired using a spin system with the given dipole coupling interaction omitted as indicated. These results reveal that the most important interaction is the heteronuclear ^{13}C-^{1}H dipole coupling, as omitting this interaction results in a trajectory with dramatically different features and an absence of the high-power PAR conditions seen in the experimental data. The homonuclear ^{1}H-^{1}H dipole coupling interactions also have a significant impact on the simulated PAR transfer conditions, but in contrast the homonuclear ^{13}C-^{13}C dipole coupling has almost no influence and omitting this parameter from the simulated spin system yields a negligible difference. The increasing agreement between experimental and simulated data as additional ^{1}H spins are included in the simulated spin system suggests that PAR magnetization transfer occurs through multiple ^{13}C-to-^{1}H-to-^{13}C pathways and that it may also occur through relayed magnetization transfer between ^{1}H nuclear spins. Given that the ^{13}C-^{13}C homonuclear dipole coupling has negligible impact on PAR magnetization transfer, the use of PAR to determine ^{13}C-^{13}C distance constraints proceeds indirectly, as corroborated by previous studies.[27, 31] However, the strong dependence on ^{13}C-^{1}H heteronuclear and ^{1}H-^{1}H homonuclear dipole couplings, suggest that quantifying PAR magnetization transfer offers the possibility of measuring ^{13}C-^{1}H and ^{1}H-^{1}H internuclear distances.

An additional interesting feature of PAR magnetization transfer in the Gly spin system is its dependence on chemical shift offsets.[27, 28, 50] These were observed using the selective PAR protocol while varying the ^{13}C transmitter offset frequency prior to PAR mixing. **Figure 3** compares experimental and simulated transmitter offset trajectories collected at the optimum PAR condition given in **Table 1**. Both the experimental and the simulated trajectory show a very strong dependence of magnetization transfer on the transmitter offset frequency. The experimental trajectory shows that maximum PAR magnetization transfer occurs with the ^{13}C transmitter offset frequency at 110 ppm, almost the exact midpoint between the ^{13}CO and ^{13}Cα resonances (177.9 ppm and 44.9 ppm,

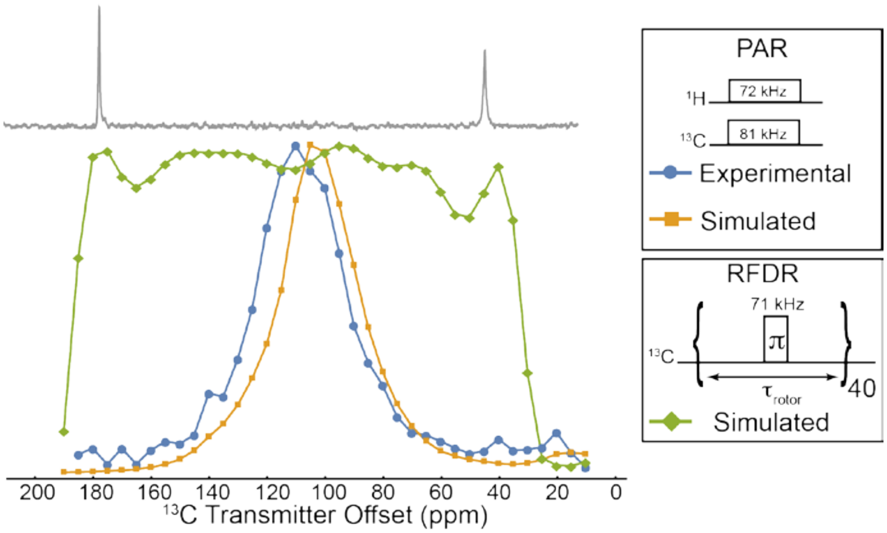

Figure 3. Magnetization transfer as a function of transmitter offset frequency for PAR (experimental and simulated, 3 milliseconds mixing time) and RFDR (simulated, 2 milliseconds mixing time). The ^{13}C spectrum of Gly is shown at top to indicate the resonance positions of the initial and final nuclei involved in the transfer.

respectively) which is unsurprising, as the SUBPAR optimization shown in **Figure 1**, which was used to determine this optimum PAR RF condition, was acquired with the ^{13}C transmitter offset at this location. Surprisingly, **Figure 3** shows that with the same $\omega_1/2\pi$ values the PAR magnetization transfer is entirely suppressed if the transmitter frequency is shifted to a value less than 60 ppm or greater than 150 ppm. Note that this is where the transmitter is still between the Cα and CO resonances. For purposes of contrast, **Figure 3** shows an analogous simulated offset profile for RFDR[15, 16] implemented with a 71 kHz ^{13}C inversion pulse and XY-8 super-cycling.[51, 52] With respect to chemical shift offsets, RFDR magnetization transfer is primarily limited by the bandwidth of the rotor-synchronized inversion pulse, and with a 71 kHz inversion pulse (3.5 μs), optimal magnetization transfer can be achieved with the transmitter offset placed anywhere between the two Gly resonances. The strong dependence of PAR magnetization transfer on the ^{13}C chemical shift offset shown in **Figure 3** illustrates the influence of second order auto-cross terms in the PAR subspace that diminish the influence of the PAR terms in the effective Hamiltonian, as predicted by the theoretical description.[27]

b. Rabi Frequency Optimization for N-acetyl-valyl-leucine (N-Ac-VL)

N-Ac-VL was chosen as the next model spin system for study as it allows for observation of multi-bond PAR magnetization transfer, and the crystal structure*[53]* and resonance assignments*[54]* have been reported previously. The sample was prepared with 10% ^{13}C,^{15}N enrichment (as described in the Materials and Methods section) to ensure that only intra-molecular polarization transfer was observed. **Figures 4** and **5** compare experimental and simulated SUBPAR optimizations for transfer from the Cα sites to a selection of different ^{13}C sites in Val and Leu, respectively. Experimental data was acquired by selectively

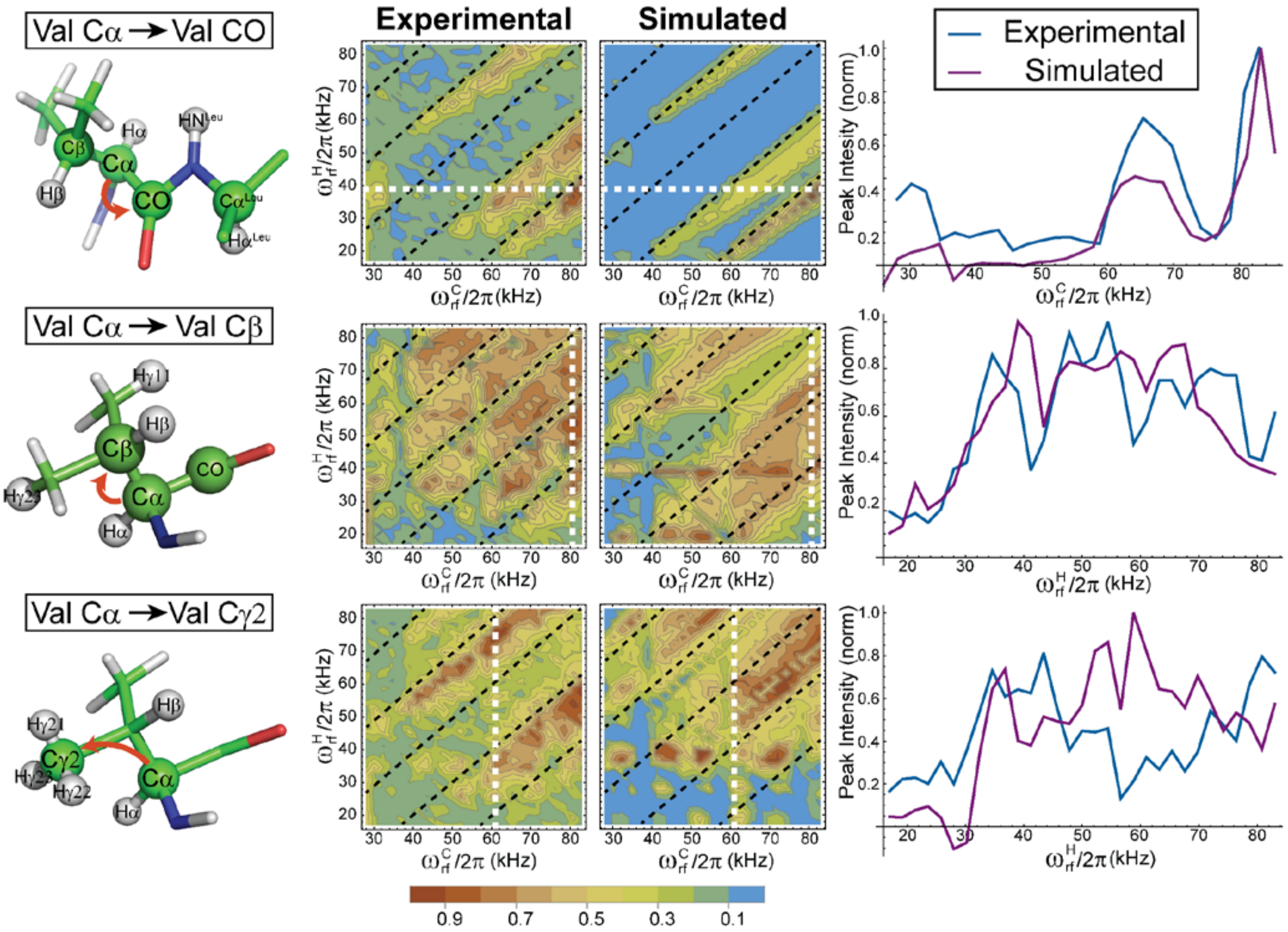

Figure 4. SUBPAR optimizations for transfer between valine nuclei in N-Ac-VL following an initial excitation of the Cα resonances. Cross-polarization conditions are indicated in the 2D RF plots by dashed black lines, and the position of the 1D traces (shown in the right column) are indicated with a horizontal or vertical dashed white line. ^{13}C and ^{1}H nuclei included in the simulated spin systems are indicated in the molecular structure by green and white spheres, respectively. The initial and final nuclei, as well as the direction of magnetization transfer are indicated in the molecular structure by orange arrows. Simulations for Val Cα -to- Val CO used 8 spins, while simulations for Val Cα -to- Val Cβ and Val Cα -to- Val Cγ2 both used 7 spins.

exciting the Cα and then observing the given signal after τ_{mix} = 3 ms of PAR mixing, and simulations were conducted accordingly.

Figures 4 and **5** illustrate satisfactory agreement between experimental and simulated data for magnetization transfer to Val CO, and Leu Cβ, moderate agreement for magnetization transfer to Val Cβ, and Leu Cγ, and a weak agreement for magnetization transfer to Val Cγ2. The optimum experimental PAR conditions for magnetization transfer to each of these sites are reported in **Table 2**. Magnetization transfer to the Val CO and Cγ2 sites is favored by Rabi frequencies occupying contour ridges parallel to but offset substantially from the static Hartmann-Hahn condition. In contrast magnetization transfer to Val Cβ and Leu Cβ, Cγ was favored by contour ridges much closer to the static Hartmann-Hahn condition.

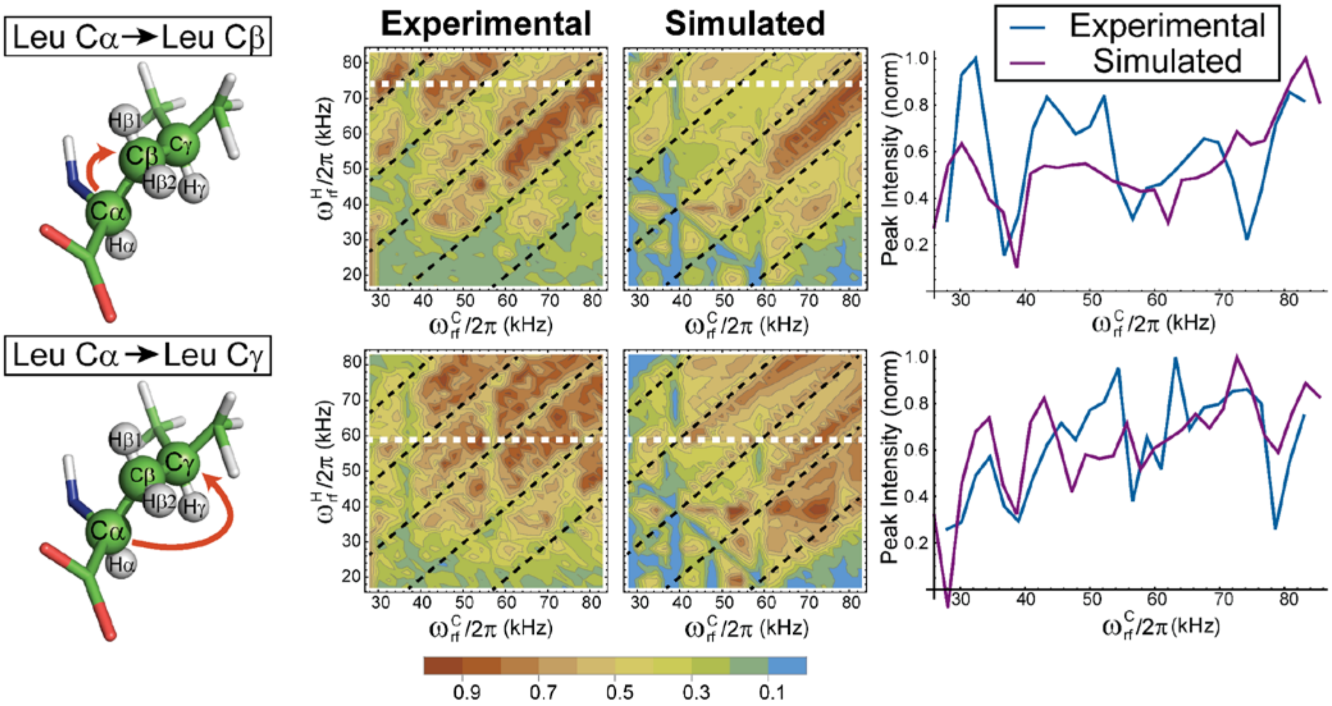

Figure 5. SUBPAR optimizations for magnetization transfer between leucine nuclei in N-Ac-VL following an initial excitation of the Cα resonances. Cross-polarization conditions are indicated in the 2D RF plots by dashed black lines, and the position of the 1D traces (shown in the right column) are indicated with a horizontal or vertical dashed white line. The initial and final nuclei, as well as the direction of magnetization transfer are indicated in the molecular structure by orange arrows. Both simulations shown used the same spin system consisting of three ^{13}C nuclei and four ^{1}H nuclei (7 total spins), as indicated by spheres in the molecular structure.

Table 2. Optimum PAR conditions in N-Ac-VL for the SUBPAR data shown in **Figures 4** and **5**.

	$\omega_{1C}/2\pi, \quad \omega_{1H}/2\pi\,(kHz)$	
Observed Spin	**Experimental**	**Simulated**
Valine CO	83, 39	83, 39
Valine Cβ	80.8, 54.4	83, 41.2
Valine Cγ2	61, 74.2	72, 58.8
Leucine Cβ	32.4, 74.2	83, 74.2
Leucine Cγ	63.2, 58.8	72, 39

The N-Ac-VL spin system exposes an inherent limitation of the 1D selective PAR sequence that is not fully appreciated with the Gly spin system, which contains only two ^{13}C spins. The SUBPAR optimization profiles shown in **Figures 4** and **5** represent the magnetization on the final spin after the PAR mixing period, but lack the frequency discrimination to exactly identify the initial spin. With initial magnetization on both the Val Cα and the Leu Cα nuclei, it is possible that the final magnetization observed at a target peak in the 1D spectrum originates from either or both of the Cα nuclei. For most of the target nuclei, the initial spin source is obvious based on relative proximity, but for magnetization transfer to the Val CO, the simulations indicate transfer from both Cα nuclei, which cannot be observed independently with 1D selective PAR. Nevertheless, implementing SUBPAR with the 1D selective PAR protocol provides a coarse optimization of PAR RF conditions for longer magnetization transfers. To collect a precise magnetization transfer profile for multi-bond transfer in a system with greater than 2 spins and multiple magnetization transfer pathways, 2D spectra are required to achieve rigorous frequency discrimination between the initial and final spins. Using 2D PAR spectra for a SUBPAR optimization would demand far more experiment time than the 1D selective PAR protocol, however 2D PAR spectra are not subject to efficiency reductions arising from selective transfer in the SPECIFIC-CP process.

Additionally, the N-Ac-VL spin system exposes the computational challenges faced when simulating PAR magnetization transfer. All field profiles were collected with 7 spins except for Val CO, where an 8th spin was included as it was found to produce a significant difference in the simulation results. Simulating SUBPAR optimization profiles with 9 or more spins was not feasible with the available computational facilities. Still, the molecular structures shown in **Figures 4** and **5** illustrate that in most situations, 7 or 8 spins is a modest representation of the surrounding nuclei. The presence of additional passive ^{13}C nuclei (that are neither the initial or final spin of the given magnetization transfer pathway) were still found to have a significant impact on the simulation results, possibly by contributing to relayed transfer or by providing a competing transfer pathway. This was seen for Val CO, and Leu Cβ, Cγ where the presence of the passive ^{13}C spins showed improved agreement between simulated and experimental data. Despite the convergence, the agreement between the simulated and experimental results could be improved.

c. Glycine Buildups

To further explore the dynamics of PAR magnetization transfer, polarization transfer trajectories (i.e. buildup curves) were collected at the optimum experimental PAR RF condition for Gly given in **Table 1**. The 1D selective PAR protocol was used as shown in **Figure 1**, as the Gly ^{13}C spectrum contains only two well-resolved peaks and therefore does not require the frequency discrimination of a 2D spectrum to identify the initial and final spin pair. Experimental peak intensities were determined by integration, and normalized by the total ^{13}C magnetization as shown in Equation 1, such that an n-spin system will continue to mix until all spins have intensity 1/n:

$$y(\omega_i, t_j) = \frac{A(\omega_i, t_j)}{\sum_{k=1}^{N} A(\omega_k, t_j)} \tag{1}$$

The simulated magnetizations were normalized with the same protocol and relaxation effects were neglected. **Figure 6A** shows experimental and simulated PAR buildup curves illustrating magnetization transfer from the Cα site to the CO site in Gly.

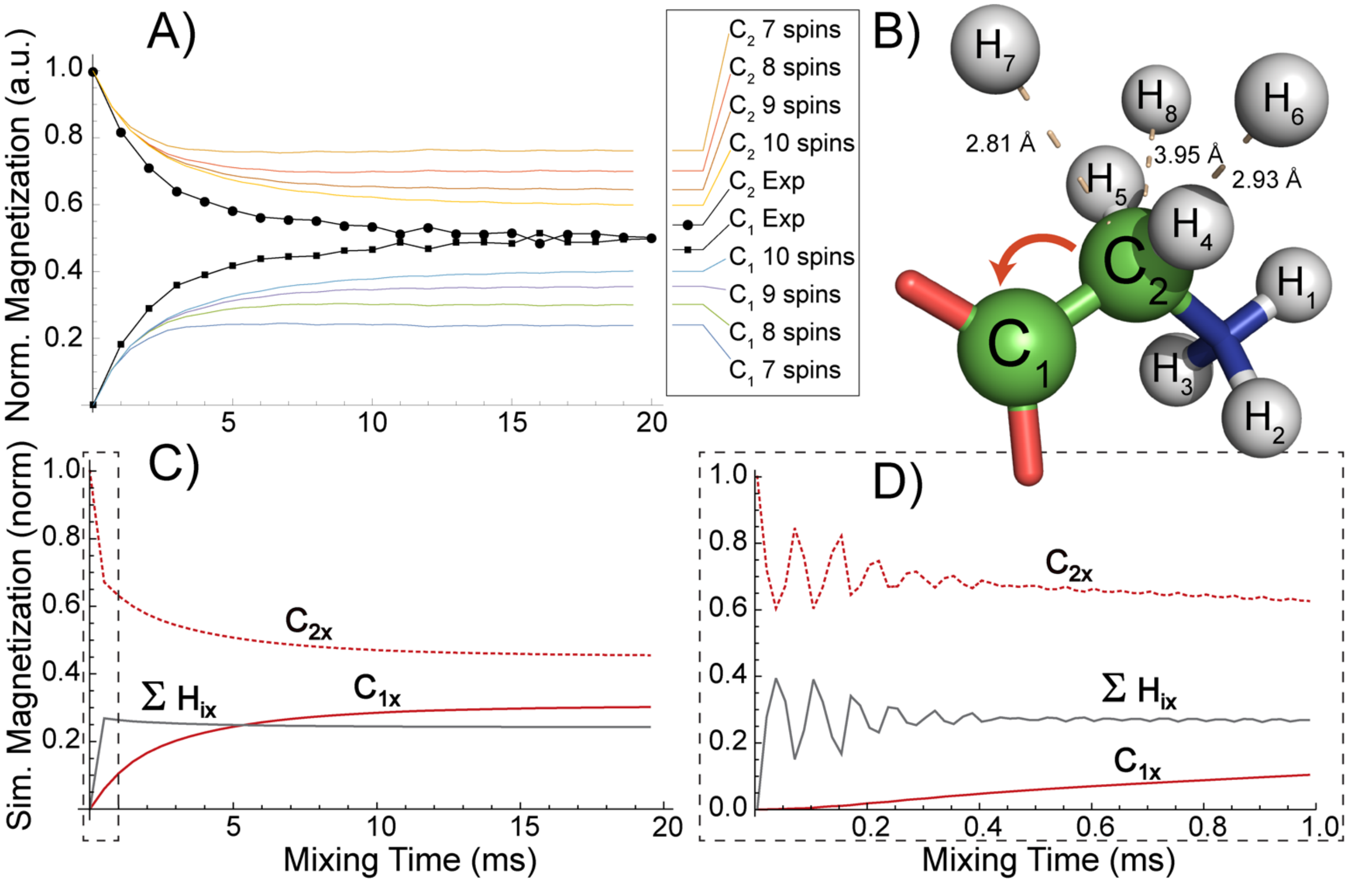

Figure 6. (A) shows the normalized magnetization trajectories of the Cα (initial) and CO (final) nuclei during PAR transfer acquired with mixing conditions set to 72.4 kHz, 80.9 kHz for ω_{rf}^{C}, ω_{rf}^{H}. (B) shows the molecular structure of the Gly simulated spin system (including ^{1}H nuclei from neighboring molecules) and the order of inclusion to yield the simulated trajectories shown in (A). (C) shows the 10-spin simulation shown in (A) indicating the absolute percentages of the total magnetization for the Cα, CO, and ^{1}H spins during the magnetization transfer process for a 10 spin system. (D) shows a zoom of the initial plot region in (C), as indicated by dashed boxes, that highlights the oscillatory behavior seen in the simulations at small mixing times, which is not seen in the experimental data.

Similar to the 1D PAR RF profiles, the experimental buildup curves show increasing agreement with simulations as additional spins were incorporated into the simulation. As shown in the **Figure 6A** the closest agreement included all of the protons in the Gly zwitterion molecular structure, and the next three closest ^{1}H's from neighboring molecules in the crystal lattice,[49] giving a 10 spin system as shown in **Figure 6B**. A single buildup calculation in a 10 spin system required approximately 4.4 hours of computation time on a 2.2 GHz quad core processor, using advanced numerical algorithms available in the most recent version of the SIMPSON simulation package.[47] Even with 10 nuclei incorporated into the simulated spin system, the results have not converged with the experimental data. **Figure 6A** illustrates how increasing the size of the simulated spin system improves the agreement between simulations and experiments, which suggests that accurate PAR simulations require the use of larger simulated spin systems, and/or suitable approximations to treat them.

It is essential to realize that the percent transfer represented in **Figure 6A** reflects the percentage of the total ^{13}C magnetization (without any ^{1}H magnetization) at a given time. This is because the PAR mechanism requires continual magnetization transfer from ^{13}C nuclei to ^{1}H nuclei and conversely from ^{1}H nuclei to ^{13}C nuclei. Thus, the total magnetization of the Gly spin system at the time of observation consists of both ^{13}C and ^{1}H magnetization, but it is not experimentally feasible to directly observe the quantity of ^{1}H magnetization (without multi-channel receiving capabilities). Therefore, this quantity exposes an experimental blind spot that can be probed with simulations. The amount of ^{13}C magnetization that is ‘leaked’ to the ^{1}H nuclei during transfer, is illustrated in **Figure 6C**, based on the 10-spin simulations. The total ^{1}H magnetization shows a steep increase within the first 1 ms before remaining relatively constant for the duration of the mixing period. Interestingly, a highly sampled simulation reveals oscillatory behavior in the magnetization transfer source and the total ^{1}H polarization during the first half-millisecond of PAR mixing (as seen in **Figure 6D**), which is reminiscent of other spin transfer processes.[24, 55, 56]

d. AGG2 and AGG3 Buildups

To explore the rates of long-range PAR magnetization transfer, the tri-peptide AGG was taken as a model spin system, given the availability of two different but analogous isotopic labeling variants (AGG2 and AGG3) that were previously used to study dipolar truncation[33] and to quantify magnetization transfer with spin diffusion.[36] A SUBPAR optimization on AGG3 yielded a 2D RF plot very similar to that of pure Gly shown in **Figure 2**, and the optimum RF condition reported in **Table 1** ($\omega_{1C}/2\pi$=77 kHz, $\omega_{1H}/2\pi =$ 81 kHz) was used to collect PAR buildup curves for the AGG samples.

Figure 7 shows PAR buildup curves that were recorded using 2D spectra to measure cross-peak intensities at each mixing time value. Peak intensities were determined by integration and normalized along the $\omega_1/2\pi$ coordinate, according to Equation 2 as this will give an intensity on each spin of 1/n when transfer has reached steady state and the polarization is shared equally by all spins receiving transfer from the same source[57]:

$$y(\omega_i,\omega_i,t_k) = \frac{A(\omega_i,\omega_j,t_k)}{\sum_{k=1}^{N} A(\omega_i,\omega_m,t_k)} \tag{2}$$

Figure 7 shows an increasing agreement between experimental and simulated data up to the maximal 10-spin simulation for both AGG2 and AGG3. All ^{13}C-^{1}H bond lengths in the simulated spin system were optimized to give the closest agreement with experimental data. Incorporating additional ^{1}H spins increases the efficiency of PAR transfer seen in the simulation (as seen in the Gly buildups in the previous section), but even with 10 spins the simulated and experimental data show a significant discrepancy, particularly in the case of long-range transfer in AGG2, as seen in **Figure 7D**.

AGG2 and AGG3 show remarkably different buildup curves for the Gly2 Cα to Gly3 CO (4.86 Å) transfer. **Figure 7B** compares cross peak intensities normalized to their maximum values (not by equation 2). For AGG2 the cross-peak intensity reaches a maximum at approximately 5 ms but for AGG3 the cross-peak intensity is still increasing after 20 ms. Since PAR is not a first order recoupling sequence and therefore is unaffected by dipolar truncation, these buildup curves suggest the presence of other effects caused by an intermediate ^{13}C spin.

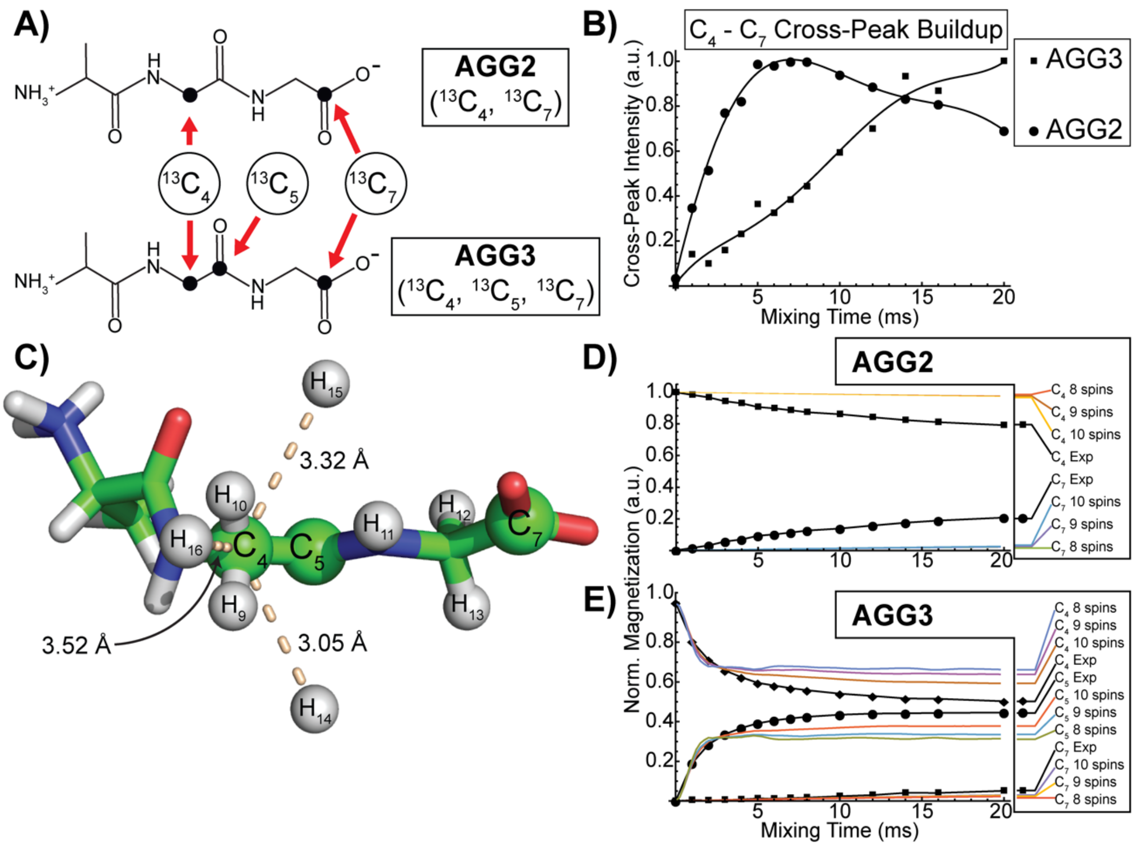

Figure 7. (A) displays the molecular formula of AGG2 and AGG3, indicating the difference in isotopic labeling. (B) shows the buildup for the C_4–C_7 cross-peak for both systems (both normalized to their maximum value), revealing distinctly different behavior. (C) illustrates the simulated spin system and the order of inclusion of different ^1H spins (including 2 from neighboring molecules in the crystal structure) that were used to generate the simulated trajectories shown in (D) and (E). (D) shows the normalized magnetization trajectories during transfer from the C4 site to the C7 site in AGG2, and (E) shows the normalized magnetization trajectories during transfer from the C4 site to the C5 and C7 sites in AGG3.

Although simulations with spin systems larger than 10 spins exceed the capabilities of our present computational resources, it is predicted that further expansion of the simulated spin system will continue to decrease the discrepancy between experimental and simulated data until a point beyond which including additional ^1H spins (that are increasingly further from the initial and final ^{13}C nuclei) will have a negligible effect. However, it is not currently possible to make a systematic estimation of the spin system size required to reach convergence in the simulations. Clearly there remain many interesting avenues to explore with respect to PAR simulations.

e. Summary of Model Systems and Simulations

The model spin systems utilized in this study provide an ideal platform for probing PAR magnetization transfer. They demonstrate the power and efficiency of the SUBPAR optimization protocol, and they are naturally conducive to simulations as they have relatively simple, and well-defined structures.

Using the selective PAR experiment, we have shown that PAR magnetization transfer has a strong dependence on chemical shift offsets as changing the transmitter frequency by 50 ppm can completely suppress PAR magnetization transfer in Gly using the optimum RF conditions, which corroborates the effect of auto-cross terms predicted by the theoretical description.

While the SUBPAR optimizations for the model systems provide an elegant realization of PAR magnetization transfer, it was not possible to achieve a completely satisfactory fit between experimental and simulated data. A comparison of experimental 2D RF plots and corresponding simulations shows a close agreement for certain spin systems, while other systems show only a minor agreement, within the limits of the available computational resources. This complements a previous study on decoupling sequences, which also found that large spin systems with many proton spins are required to achieve accurate simulated results.[58] It is uncertain if the availability of more powerful computational resources, or alternative simulation platforms[59, 60] will enable precise simulations of PAR magnetization transfer, as many of the spin transfer pathways interrogated in this study converged upon a consistent result at a limit of 7 spins, producing a trajectory that deviates significantly from the experimental data.

The disagreement between experimental and simulated results suggests the influence of both coherent and stochastic processes during PAR magnetization transfer. The current simulations incorporate chemical shift and dipole coupling terms with the effect of RF irradiation, but they do not include relaxation effects. Thus, one could attribute the given discrepancies between simulations and experiment to the influence of stochastic effects. The relative influence of these factors cannot easily be assessed in a uniformly labeled peptide sample, as $T_{1\rho}$ relaxation rates are not easily isolated and measured in this setting, particularly with simultaneous irradiation on both channels.

Despite the quantitative discrepancies with experimental data, the PAR simulations offer a wealth of information concerning the underlying details of the magnetization transfer mechanism. For example, a systematic evaluation of dipole interactions reveals that the most influential is ^{13}C-^{1}H, which could facilitate a molecular fitting protocol by measuring heteronuclear couplings. Comparing the experimental and simulated SUBPAR optimizations reveals many intriguing features, including the singular association of each spin system to a unique RF-polarization transfer topology. Furthermore, the SUBPAR optimizations show a strong, qualitative agreement between experiment and simulation suggesting that a 1D PAR RF frequency sweep (where one channel is maintained at a constant RF intensity while the other channel is swept across a range of values) could be used for a qualitative fitting procedure. While the PAR buildup curves are seemingly simple in form, they offer the possibility of a kinetic model for magnetization transfer to further characterize the underlying spin physics. Future fundamental investigations of this nature will further advance the understanding of PAR, thereby increasing the quantitative capabilities and inspiring related techniques to obtain precise internuclear distance measurements.

II. PAR in Microcrystalline and Amyloid Protein Samples

a. GB1 and $M_0A\beta_{1\text{-}42}$ RF Optimization

The Gly and N-Ac-VL PAR SUBPAR optimizations shown in the previous sections allow a detailed investigation of site-specific PAR polarization transfer observed in well-resolved 1D spectra. However, these peptide samples represent model spin systems without complex features like α-helices and β-sheets that are defining features of protein structure and function. Thus, the optimum PAR conditions for Gly and N-Ac-VL reported in the previous sections are not necessarily representative of

PAR magnetization transfer in a *real* protein. Accordingly, to explore the regime of protein samples, SUBPAR optimizations were recorded for crystalline GB1 and $M_0A\beta_{1\text{-}42}$ fibrils. **Figure 8** shows the results of a SUBPAR optimization with initial magnetization on the Cα resonances. An analogous optimization for transfers beginning on the CO resonances is given in SI2. The transferred magnetization shown in the contour plots reflects the integrated intensities of the specified target regions, and is therefore representative of the general (non-site specific) magnetization transfer to the collective resonances in that region. The selectively excited initial region, and the different target regions are shaded in the 1D spectra, and the limits of these regions are given in **Table 3**, along with the maxima of each 2D RF contour plot, corresponding to optimum transfer conditions.

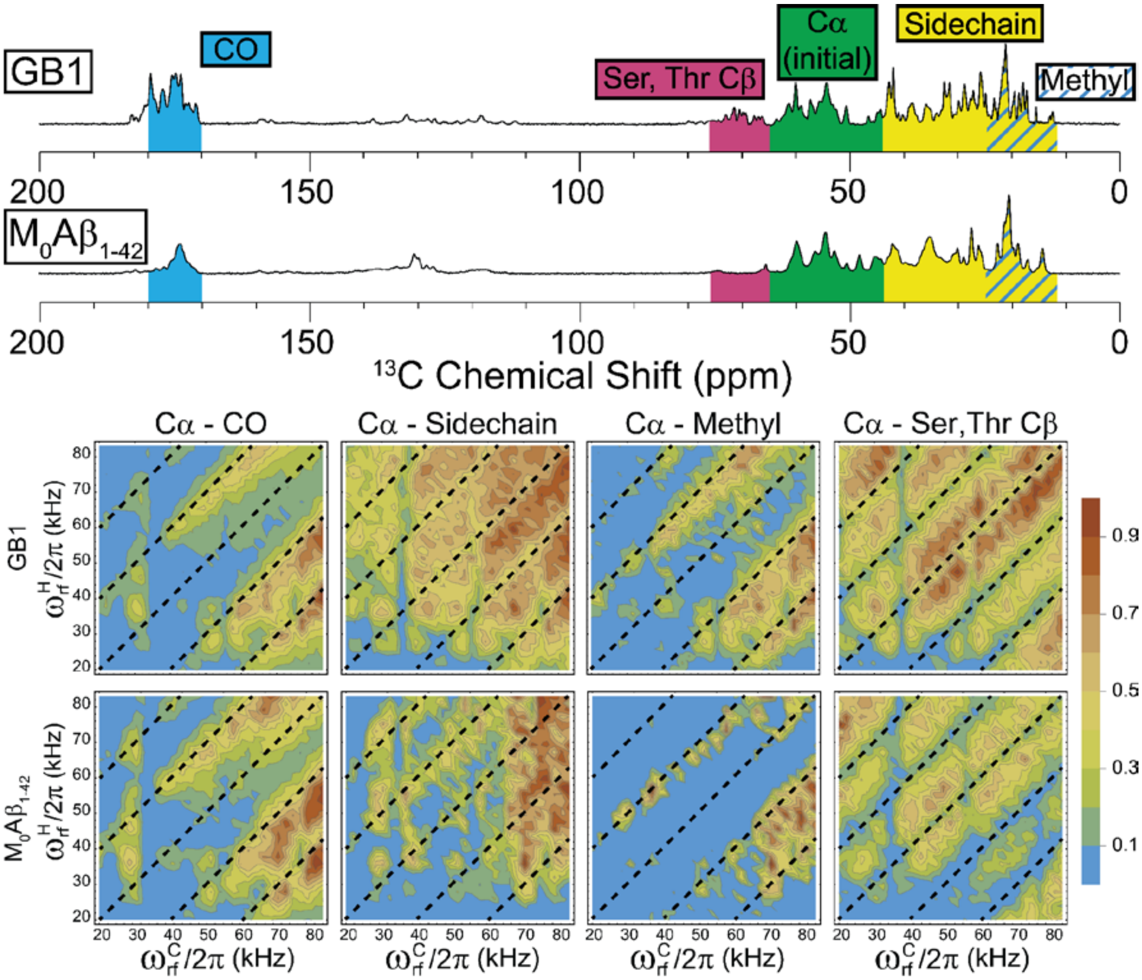

Figure 8. Top row indicates the initial region (Cα) and the different target regions of the 1D spectra used for SUBPAR optimizations on GB1 and $M_0A\beta_{1\text{-}42}$. Magnetization transfer was determined by integrating the target regions for each spectrum acquired at a different ω_{rf}^{C}, ω_{rf}^{H} condition.

The experimental SUBPAR optimizations presented in **Figure 8** are not intended for comparison with simulation as the 1D selective PAR spectra acquired from GB1 and $M_0A\beta_{1-42}$ lack the resolution and the frequency discrimination to identify initial and final spin pairs for the many magnetization transfer pathways. Rather they provide an approximate but detailed calibration of experimental PAR RF conditions. For example, to observe correlations between Cα and sidechain ^{13}C nuclei in $M_0A\beta_{1-42}$, a suitable choice of PAR RF conditions is $\omega_{1C}/2\pi =$ 74 kHz, $\omega_{1H}/2\pi =$ 57.4 kHz.

Table 3. Optimum PAR RF conditions for magnetization transfer from the Cα/CO nuclei to the specified observed regions in GB1 and $M_0A\beta_{1-42}$ as determined by the SUBPAR protocol.

		Optimum PAR Condition $\omega_{1C}/2\pi,\ \omega_{1H}/2\pi\ (kHz)$	
Excited Region	**Observed Region**	**GB1**	**$A\beta_{1-42}$**
Cα (44-65 ppm)	CO (170-180 ppm)	83, 41.7	72.2, 35.8
	Sidechain (11-44 ppm)	67.3, 59.4	74, 57.4
	Methyl (11-24.5 ppm)	83, 59.4	63.2, 35.8
	Ser, Thr Cβ (65-75 ppm)	79.1, 73.2	20, 75.1
CO (170-180 ppm)	Cα (44-65 ppm)	81, 37.7	72.4, 55.2
	Sidechain (11-44 ppm)	79.1, 55.4	59.7, 83
	Methyl (11-24.5 ppm)	79.1, 57.4	59.7, 83
	Ser, Thr Cβ (65-75 ppm)	22, 83	20, 79.3

b. $M_0A\beta_{1\text{-}42}$ Buildups and Structural Relevance

To explore the structural implications of PAR magnetization transfer in $M_0A\beta_{1\text{-}42}$, a series of buildup curves were assembled by acquiring 2D PAR spectra at three of the different conditions reported in **Table 3**, with mixing times ranging from 1 to 12 milliseconds. **Figure 9** shows sample 2D spectra collected with the Cα-to-sidechain conditions at three different mixing times. The three PAR conditions used to collect build-up curves (optimal conditions for Cα-to-CO, Cα-to-sidechain, and Cα-to-methyl transfer) were chosen to generate the maximum number of cross-peaks, but also to generate cross-peaks corresponding to long-range transfer. Resonance assignments were taken from a recent publication,[45] and internuclear distances were taken from the 5KK3 PDB structure.[6] All build-up curves show the trajectory of cross-peak intensity (normalized only to the maximum value), as this system could not be normalized according to equation 2, as it was not possible to resolve and integrate diagonal peaks due to spectral crowding. Nearly all of the PAR buildup curves observed in this study were mono- or bi-exponential in character, and signify a qualitative description of the initial buildup and subsequent decay of the transferred magnetization. Fitting curves were then calculated with the bi-exponential formula given in Equation 3, providing a set of kinetic parameters that model the time dependence of the data:

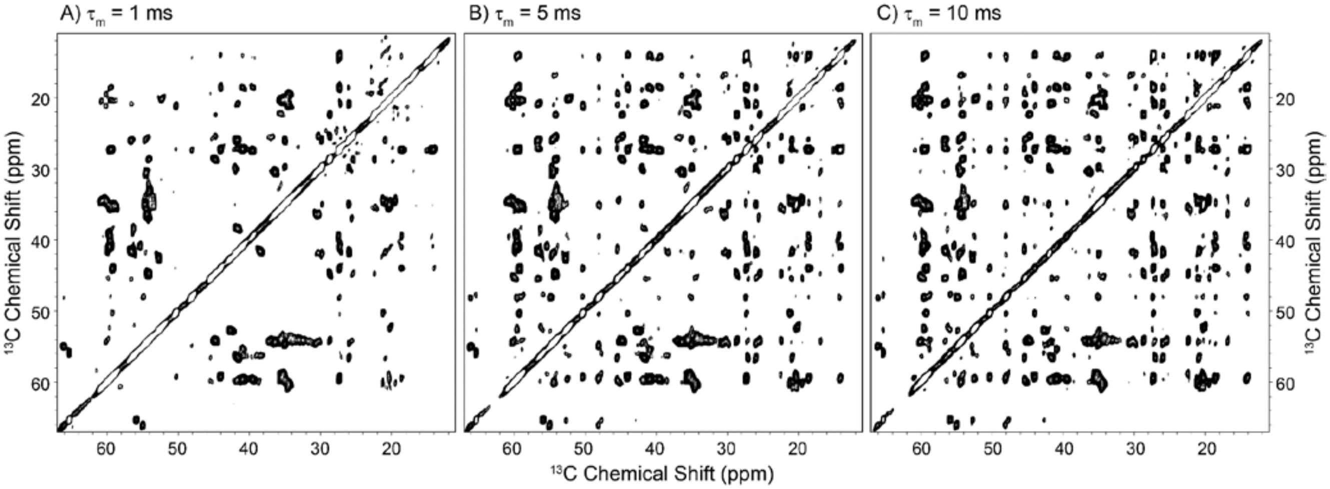

Figure 9. Aliphatic region of 2D PAR spectra from $M_0A\beta_{1\text{-}42}$ acquired at the Ca-to-sidechain optimal condition given in **Table 3** for variable mixing times. (A) was acquired with 1 ms PAR mixing and shows primarily short-range contacts between bonded, or otherwise close ^{13}C pairs. (B) was acquired with 5 ms PAR mixing and shows a mixture of short-range and long-range contacts with different intensities. (C) was acquired with 20 ms PAR mixing and shows extensive magnetization transfer, with numerous cross peaks for a broad range of contacts.

$$y = a_1(1-e^{-k_1 t}) + a_2(1-e^{-k_2 t}) \tag{3}$$

Figure 10 shows a series of buildup curves for intra-residue magnetization transfer pathways. In each build-up curve the numerical fit provides an excellent prediction of the data points. A qualitative comparison is obtained by analyzing the relative build-up rate, the position of the maximum (if a maximum occurs), and the relative decay rate, across all three conditions. A comparison of the intra-

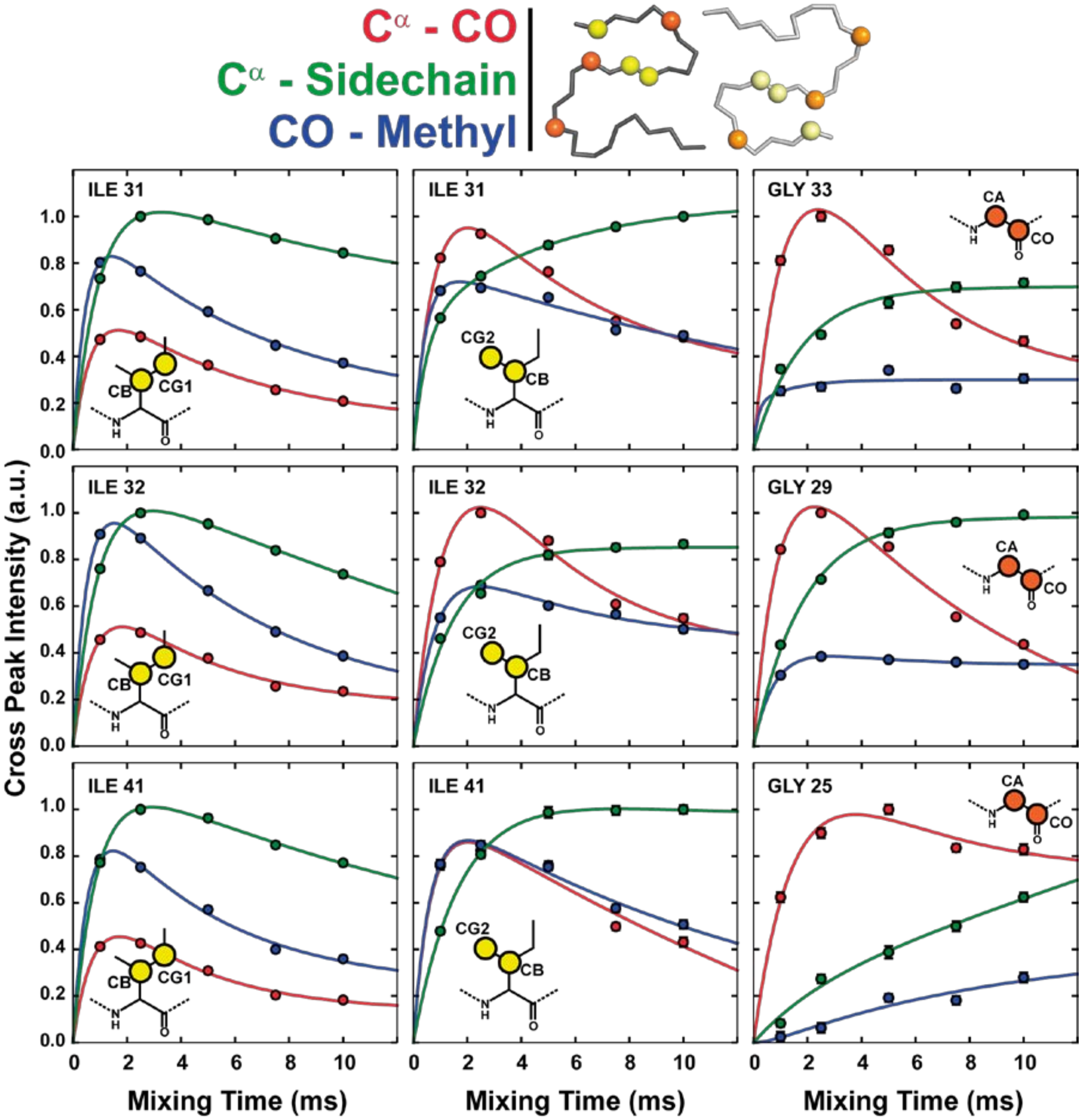

Figure 10. Intra-residue PAR build-up curves showing corresponding magnetization transfer pathways for isoleucine and glycine in $M_0A\beta_{1-42}$. The schematic molecular structure (top) shows the residue positions where the yellow spheres indicate Ile and the orange spheres indicate Gly. The build-up curves demonstrate typical behaviors across the different $\omega_{1C}/2\pi$, $\omega_{1H}/2\pi$ PAR conditions.

residue build-up curves for analogous transfer pathways in similar residues yields similarity in some situations (i.e. Cα to CO transfer in Gly29 and Gly33 and Cβ to Cγ1 in Ile31 and Ile41, and a different character in other situations (i.e. Cβ to Cγ2 transfer in Ile32 and Ile41). This is despite the fact that all buildup curves shown in **Figure 10** reflect transfer between directly bonded ^{13}C nuclei, and therefore the same (~1.45 A) distance. This suggests that PAR magnetization transfer is affected by the previously mentioned stochastic effects (such as relaxation and dynamic processes), but also by a local environment with a relatively large encompassing diameter.

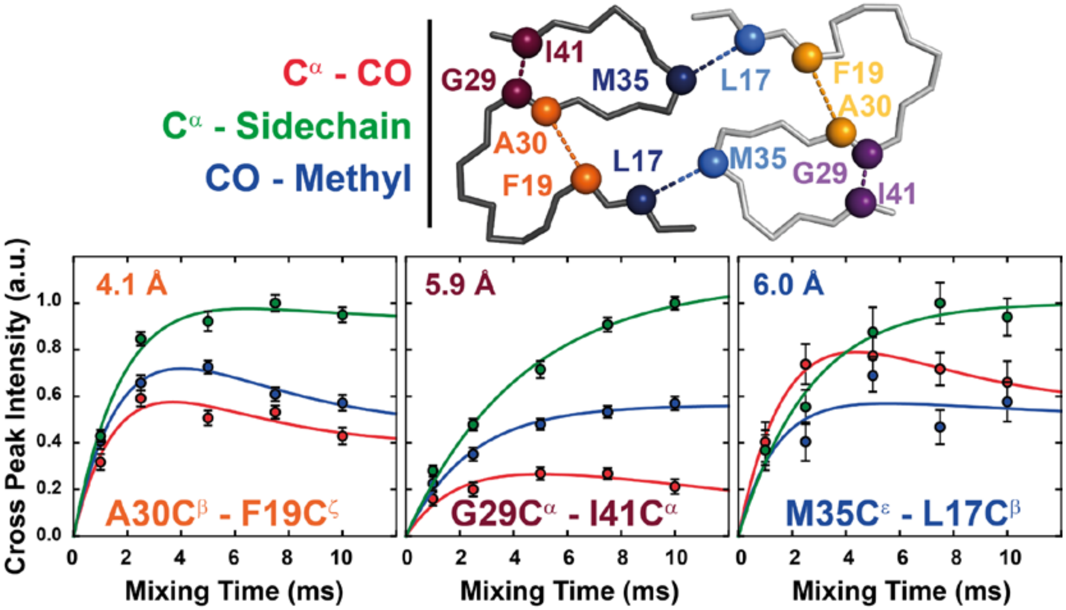

Figure 11. Inter-residue PAR build-up curves at three different $\omega_{1C}/2\pi$, $\omega_{1H}/2\pi$ PAR conditions with a $M_0A\beta_{1-42}$ structure illustrating the structural significance of the magnetization transfer. The dashed lines illustrating the internuclear distances are not drawn to scale, and are only offered as a visual aid.

Figure 11 shows a series of build-up curves for inter-residue magnetization transfer pathways, including three long-distance contacts of 4.1 Å, 5.9 Å and 6.0 Å. These build-up curves were chosen to represent a collection of similar distances and local environments. As seen with the intra-residue buildup curves, the inter-residue magnetization transfer displays rather different behavior across different PAR conditions, and different internuclear distances.

Figure 12 shows a scatter plot relating fitting parameters in $M_0A\beta_{1-42}$ to internuclear distances for all PAR build-up curves that allowed for a reasonable fit of the experimental data. Build-up curves that were not accurately predicted by equation 3 (due to low sensitivity, erratic data points, or other problems) were excluded. The scatter plots reveal a distribution of internuclear distances with PAR. There are many contacts with similar internuclear distances that have completely different fitting parameters, and there are many contacts with the same fitting parameters for completely different internuclear distances, and there are no well-defined trends. Nevertheless, this information offers a valuable summary of optimal PAR mixing times and the maximum observable internuclear distances at three different PAR conditions, for use in future structural studies.

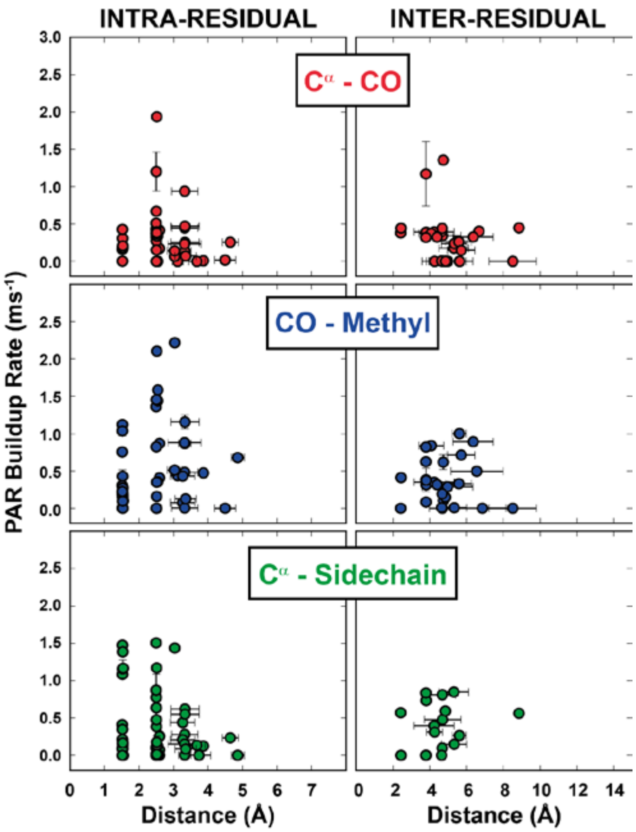

Figure 12. Scatter plots correlating PAR buildup rates and internuclear distances for intra-residue and inter-residue magnetization transfer in $M_0A\beta_{1-42}$, at the three different $\omega_{1C}/2\pi$, $\omega_{1H}/2\pi$ PAR conditions examined in this study.

Conclusions

This paper provides a description of SUBPAR, the first complete $\omega_{1C}/2\pi$, $\omega_{1H}/2\pi$ PAR experimental optimization, the absence of which has previously been a significant impediment to the application and analysis of the PAR experiment. While the SUBPAR protocol provides a useful means of optimization, it is limited in its applicability, due to the inability of SPECIFIC-CP to excite a single Cα/CO resonance when many are present. One could use selective pulses to excite a single resonance[61] and subsequently observe PAR transfer,[28] although this approach would require a careful calibration and would still sacrifice magnetization, much like SPECIFIC-CP.

The SUBPAR optimizations presented here for model peptides and proteins confirm that optimum RF conditions are frequently found at slightly mismatched $\omega_{1C}/2\pi$, $\omega_{1H}/2\pi$ values. However, it was also shown that the optimum conditions for some magnetization transfer pathways can occur at substantially mismatched values and therefore all of these conditions need to be considered when initiating a PAR experiment. Furthermore, the chemical shift offset has a large impact on PAR magnetization transfer and should also be given sufficient consideration.

This report offers a systematic analysis of PAR magnetization transfer by comparing simulations and experiments on model compounds. These results demonstrate that PAR magnetization transfer occurs via relayed transfer through a ^{1}H nuclear spin network, and is therefore a multispin process that necessitates simulations with numerous nuclei. A detailed comparison of experimental and simulated PAR data suggests that the magnetization transfer process depends primarily on local proton density, and is invariant to the ^{13}C-^{13}C homonuclear dipolar coupling. Given the limited computational resources used in this study, it was not possible to simulate the experimental data in detail, suggesting that a more elaborate mathematical framework (that incorporates relaxation and other stochastic effects) is required for highly accurate simulations.

The SUBPAR optimizations provided for protein samples (GB1, and $M_0A\beta_{1-42}$) offer a coarse calibration procedure to maximize the quantity and intensity of cross-peaks in a 2D spectrum. The optimum conditions for different transfer pathways were used to record buildup curves for $M_0A\beta_{1-42}$, which provide an additional empirical calibration for maximizing magnetization transfer. While the buildup curves are easily fit with a generic multi-exponential formula, the fitting parameters cannot be closely correlated to internuclear distances, even for similar residue types, thereby supporting the conjecture that PAR magnetization transfer is dictated by the local proton density. Given the widely varied character of PAR buildup curves seen for $M_0A\beta_{1-42}$, that are heavily affected by different factors including local proton architecture (amongst others), it is useful to screen different conditions as well as different mixing times to deduce long-range information in larger biomacromolecules.

This systematic evaluation of PAR has provided insight on the underlying polarization transfer mechanisms and represents a large step towards quantifying homonuclear magnetization transfer processes in peptide and protein samples. This investigation provides a foundation to inspire variants of the PAR sequence to obtain structural restraints and potentially internuclear distance measurements. With these results, PAR will prove extremely useful for high-resolution structural studies of membrane proteins, amyloid fibrils and other biological macromolecules that are propitious to solid-state NMR.

Acknowledgments

The authors thank Enrico Ravera and Eugenio Daviso for their help and encouragement, and Zdeněk Tošner for assistance with the SIMPSON simulations. This research was supported by the National Institutes of Health (EB-001960, AG-058504, and EB-002026). R.S. is funded by a DFG research fellowship (SI2105/1-1).

Supporting Information

SI1 SIMPSON Script for PAR 2D RF Optimization on Glycine
SI2 SUBPAR Optimizations for Transfer from CO Region in GB1 and $M_0A\beta_{1\text{-}42}$

References

(1) Castellani, F.; van Rossum, B.; Diehl, A.; Schubert, M.; Rehbein, K.; Oschkinat, H. Structure of a protein determined by solid-state magic-angle-spinning NMR spectroscopy. *Nature* **2002**, *420*, 98-102.
(2) Franks, W. T.; Zhou, D. H.; Wylie, B. J.; Money, B. G.; Graesser, D. T.; Frericks, H. L.; Sahota, G.; Rienstra, C. M. Magic-angle spinning solid-state NMR spectroscopy of the β1 immunoglobulin binding domain of protein G (GB1): ^{15}N and ^{13}C chemical shift assignments and conformational analysis. *J. Am. Chem. Soc.* **2005**, *127*, 12291-12305.
(3) Nieuwkoop, A. J.; Wylie, B. J.; Franks, W. T.; Shah, G. J.; Rienstra, C. M. Atomic resolution protein structure determination by three-dimensional transferred echo double resonance solid-state nuclear magnetic resonance spectroscopy. *J. Chem. Phys.* **2009**, *131*, 095101.
(4) Bertini, I.; Bhaumik, A.; De Paëpe, G.; Griffin, R. G.; Lelli, M.; Lewandowski, J. R.; Luchinat, C. High-resolution solid-state NMR structure of a 17.6 kDa protein. *J. Am. Chem. Soc.* **2010**, *132*, 1032-1040.
(5) Colvin, M. T.; Silvers, R.; Frohm, B.; Su, Y.; Linse, S.; Griffin, R. G. High resolution structural characterization of Aβ42 amyloid fibrils by MAS NMR. *J. Am. Chem. Soc.* **2015**, *137*, 7509–7518
(6) Colvin, M. T.; Silvers, R.; Ni, Q. Z.; Can, T. V.; Sergeyev, I.; Rosay, M.; Donovan, K. J.; Michael, B.; Wall, J.; Linse, S.; et al. Atomic resolution structure of monomorphic Aβ42 amyloid fibrils. *J. Am. Chem. Soc.* **2016**, *138*, 9663–9674.
(7) Schütz, A. K.; Vagt, T.; Huber, M.; Ovchinnikova, O. Y.; Cadalbert, R.; Wall, J.; Güntert, P.; Böckmann, A.; Glockshuber, R.; Meier, B. H. Atomic-resolution three-dimensional structure of amyloid β fibrils bearing the Osaka mutation. *Angew. Chem. Int. Ed.* **2015**, *54*, 331-335.
(8) Wasmer, C.; Lange, A.; Van Melckebeke, H.; Siemer, A. B.; Riek, R.; Meier, B. H. Amyloid fibrils of the HET-s(218-289) prion form a beta solenoid with a triangular hydrophobic core. *Science* **2008**, *319*, 1523-1526.
(9) Wälti, M. A.; Ravotti, F.; Arai, H.; Glabe, C. G.; Wall, J. S.; Böckmann, A.; Güntert, P.; Meier, B. H.; Riek, R. Atomic-resolution structure of a disease-relevant Aβ(1–42) amyloid fibril. *Proc. Natl. Acad. Sci. U.S.A.* **2016**, *113*, E4976–E4984.
(10) Andreas, L. B.; Reese, M.; Eddy, M. T.; Gelev, V.; Ni, Q. Z.; Miller, E. A.; Emsley, L.; Pintacuda, G.; Chou, J. J.; Griffin, R. G. Structure and function of the influenza A M218-60 dimer of dimers. *J. Am. Chem. Soc.* **2015**, *137*, 14877-14866.
(11) Tuttle, M. D.; Comellas, G.; Nieuwkoop, A. J.; Covell, D. J.; Berthold, D. A.; Kloepper, K. D.; Courtney, J. M.; Kim, J. K.; Barclay, A. M.; Kendall, A.; et al. Solid-state NMR structure of a pathogenic fibril of full-length human alpha-synuclein. *Nat. Struct. Mol. Biol.* **2016**, *23*, 409-415.
(12) Szevernyi, N.; Sullivan, M.; Maciel, G. Observation of spin exchange by two-dimensional fourier-transform ^{13}C cross polarizaton-magic angle spinning. *J. Magn. Reson.* **1982**, *47*, 462-475.
(13) Raleigh, D. P.; Levitt, M. H.; Griffin, R. G. Rotational resonance in solid state NMR. *Chem. Phys. Lett.* **1988**, *146*, 71-76.
(14) Levitt, M. H.; Raleigh, D. P.; Creuzet, F.; Griffin, R. G. Theory and simulations of homonuclear spin pair systems in rotating solids. *J. Chem. Phys.* **1990**, *92*, 6347-6364.
(15) Bennett, A. E.; Griffin, R. G.; Ok, J. H.; Vega, S. Chemical shift correlation spectroscopy in rotating solids: radio frequency ‐ driven dipolar recoupling and longitudinal exchange. *J. Chem. Phys.* **1992**, *96*, 8624-8627.
(16) Bennett, A. E.; Rienstra, C. M.; Griffiths, J. M.; Zhen, W.; Lansbury, P. T.; Griffin, R. G. Homonuclear radio frequency-driven recoupling in rotating solids. *J. Chem. Phys.* **1998**, *108*, 9463-9479.
(17) Verel, R.; Ernst, M.; Meier, B. H. Adiabatic dipolar recoupling in solid-state NMR: the DREAM scheme. *J. Magn. Reson.* **2001**, *150*, 81-99.

(18) Takegoshi, K.; Nakamura, S.; Terao, T. C-13-H-1 dipolar-assisted rotational resonance in magic-angle spinning NMR. *Chem. Phys. Lett.* **2001**, *344*, 631-637.

(19) Nielsen, N. C.; Bildsoe, H.; Jakobsen, H. J.; Levitt, M. H. Double-quantum homonuclear rotary resonance: efficient dipolar recovery in magic-angle spinning nuclear magnetic resonance. *J. Chem. Phys.* **1994**, *101*, 1805-1812.

(20) Sun, B. Q.; Costa, P. R.; Kocisko, D.; Lansbury, P. T.; Griffin, R. G. Internuclear distance measurements in solid-state nuclear- magnetic-resonance - dipolar recoupling via rotor synchronized spin locking. *J. Chem. Phys.* **1995**, *102*, 702-707.

(21) Baldus, M. A.; Petkova, A. T.; Herzfeld, J.; Griffin, R. G. Cross polarization in the tilted frame: assignment and spectral simplification in heteronuclear spin systems. *Mol. Phys.* **1997**, *95*, 1197-1207.

(22) Hohwy, M.; Rienstra, C. M.; Jaroniec, C. P.; Griffin, R. G. Fivefold symmetric homonuclear dipolar recoupling in rotating solids: application to double quantum spectroscopy. *J. Chem. Phys.* **1999**, *110*, 7983-7992.

(23) Hohwy, M.; Rienstra, C. M.; Griffin, R. G. Band-selective homonuclear dipolar recoupling in rotating solids. *J. Chem. Phys.* **2002**, *117*, 4973-4987.

(24) Gullion, T.; Schaefer, J. Rotational-echo double-resonance NMR. *J. Magn. Reson.* **1989**, *81*, 196-200.

(25) Jaroniec, C. P.; Tounge, B. A.; Rienstra, C. M.; Herzfeld, J.; Griffin, R. G. Recoupling of heteronuclear dipolar interactions with rotational-echo double-resonance at high magic-angle spinning frequencies. *J. Magn. Reson.* **2000**, *146*, 132-139.

(26) Jaroniec, C. P.; Filip, C.; Griffin, R. G. 3D TEDOR NMR experiments for the simultaneous measurement of multiple carbon-nitrogen distances in uniformly C-13, N-15- labeled solids. *J. Am. Chem. Soc.* **2002**, *124*, 10728-10742.

(27) DePaëpe, G.; Lewandowski, J. R.; Loquet, A.; Böckmann, A.; Griffin, R. G. Proton assisted recoupling and protein structure determination. *J. Chem. Phys.* **2008**, *129*, 245101.

(28) Giffard, M.; Hediger, S.; Lewandowski, J. R.; Bardet, M.; Simorre, J. P.; Griffin, R. G.; De Paepe, G. Compensated second-order recoupling: application to third spin assisted recoupling. *Phys. Chem. Chem. Phys.* **2012**, *14*, 7246-7255.

(29) Lewandowski, J. R.; De Paepe, G.; Eddy, M. T.; Griffin, R. G. N-15-N-15 Proton Assisted Recoupling in Magic Angle Spinning NMR. *J. Am. Chem. Soc.* **2009**, *131*, 5769-5776.

(30) Lewandowski, J. R.; De Paepe, G.; Eddy, M. T.; Struppe, J.; Maas, W.; Griffin, R. G. Proton assisted recoupling at high spinning frequencies. *J. Phys. Chem. B* **2009**, *113*, 9062-9069.

(31) Paul, S.; Takahashi, H.; Hediger, S.; De Paëpe, G. (2015) Chapter Three - Third Spin-Assisted Recoupling in SSNMR: Theoretical Insights and Practicable Application to Biomolecular Structure Determination, In *Annual Reports on NMR Spectroscopy* (Graham, A. W., Ed.), pp 93-142, Academic Press.

(32) Wälti, M. A.; Ravotti, F.; Arai, H.; Glabe, C. G.; Wall, J. S.; Böckmann, A.; Güntert, P.; Meier, B. H.; Riek, R. Atomic-resolution structure of a disease-relevant Aβ(1–42) amyloid fibril. *Proc. Natl. Acad. Sci. U.S.A.* **2016**, *113*, E4976-E4984.

(33) Bayro, M. J.; Huber, M.; Ramachandran, R.; Davenport, T. C.; Meier, B. H.; Ernst, M.; Griffin, R. G. Dipolar truncation in magic-angle spinning NMR recoupling experiments. *J. Chem. Phys.* **2009**, *130*.

(34) Szeverenyi, N. M.; Sullivan, M. J.; Maciel, G. E. Observation of spin exchange by two-dimensional fourier transform ^{13}C cross polarization-magic-angle spinning. *J. Magn. Reson.* **1982**, *47*, 462-475.

(35) Suter, D.; Ernst, R. R. Spectral spin diffusion in the presence of an extraneous dipolar reservoir. *Phys. Rev. B* **1982**, *25*, 6038-6041.

(36) Veshtort, M.; Griffin, R. G. Proton-driven spin diffusion in rotating solids via reversible and irreversible quantum dynamics. *J. Chem. Phys.* **2011**, *135*, 134509.

(37) Hartmann, S. R.; Hahn, E. L. Nuclear double resonance in rotating frame. *Phys. Rev.* **1962**, *128*, 2042-&.
(38) Pines, A.; Gibby, M. G.; Waugh, J. S. Proton-enhanced NMR of dilute spins in solids. *J. Chem. Phys.* **1973**, *59*, 569-590.
(39) Bayro, M. J.; Ramachandran, R.; Caporini, M. A.; Eddy, M. T.; Griffin, R. G. Radio frequency-driven recoupling at high magic-angle spinning frequencies: homonuclear recoupling sans heteronuclear decoupling. *J. Chem. Phys.* **2008**, *128*, 052321.
(40) Eddy, M. T.; Ong, T.-C.; Clark, L.; Teijido, O.; Wel, P. C. A. v. d.; Garces, R.; Wagner, G.; Rostovtseva, T. K.; Griffin, R. G. Lipid dynamics and protein−lipid interactions in 2D crystals formed with the β-barrel integral membrane protein VDAC1. *J. Am. Chem. Soc.* **2012**, *134*, 6375−6387.
(41) Eddy, M. T.; Andreas, L.; Teijido, O.; Su, Y.; Clark, L.; Noskov, S. Y.; Wagner, G.; Rostovtseva, T. K.; Griffin, R. G. Magic angle spinning nuclear magnetic resonance characterization of voltage-dependent anion channel gating in two-dimensional lipid crystalline bilayers. *Biochemistry* **2015**, *54*, 994-1005.
(42) Eddy, M. T.; Belenky, M.; Sivertsen, A. C.; Griffin, R. G.; Herzfeld, J. Selectively dispersed isotope labeling for protein structure determination by magic angle spinning NMR. *J. Biomol. NMR* **2013**, *57*, 129-139.
(43) Petkova, A. T.; Baldus, M.; Belenky, M.; Hong, M.; Griffin, R. G.; Herzfeld, J. Backbone and side chain assignment strategies for multiply labeled membrane peptides and proteins in the solid state. *J. Magn. Reson.* **2003**, *160*, 1-12.
(44) Baldus, M.; Petkova, A. T.; Herzfeld, J.; Griffin, R. G. Cross polarization in the tilted frame: assignment and spectral simplification in heteronuclear spin systems. *Mol. Phys.* **1998**, *95*, 1197-1207.
(45) Colvin, M. T.; Silvers, R.; Frohm, B.; Su, Y.; Linse, S.; Griffin, R. G. High resolution structural characterization of Aβ42 amyloid fibrils by magic angle spinning NMR. *J. Am. Chem. Soc.* **2015**, *137*, 7509-7518.
(46) Bak, M.; Rasmussen, J. T.; Nielsen, N. C. SIMPSON: A general simulation program for solid-state NMR spectroscopy. *J. Magn. Reson.* **2000**, *147*, 296-330.
(47) Tosner, Z.; Andersen, R.; Stevenss, B.; Eden, M.; Nielsen, N. C.; Vosegaard, T. Computer-intensive simulation of solid-state NMR experiments using SIMPSON. *J. Magn. Reson.* **2014**, *246*, 79-93.
(48) Vosegaard, T.; Malmendal, A.; Nielsen, N. C. The flexibility of SIMPSON and SIMMOL for numerical simulations in solid- and liquid-state NMR spectroscopy. *Chemical Monthly* **2002**, *133*, 1555-1574.
(49) Jönsson, P. G.; Kvick, Å. Precision neutron diffraction structure determination of protein and nucleic acid components. III. The crystal and molecular structure of the amino acid [alpha]-glycine. *Acta Crystallogr. B* **1972**, *B28*, 1827-1833.
(50) DePaëpe, G.; Lewandowski, J. R.; Loquet, A.; Eddy, M.; Megy, S.; Böckmann, A.; Griffin, R. G. Heteronuclear proton assisted recoupling. *J. Chem. Phys.* **2011**, *134*, 095101.
(51) Gullion, T.; Baker, D. B.; Conradi, M. S. New, compensated Carr-Purcell sequences. *J. Magn. Reson.* **1990**, *89*, 479-484.
(52) Lizak, M. J.; Gullion, T.; Conradi, M. S. Measurement of like-spin dipole couplings. *J. Magn. Reson.* **1991**, *91*, 254-260.
(53) Carroll, P. J.; Stewart, P. L.; Opella, S. J. Structures of two model peptides: N-acetyl-d,l-valine and N-acetyl-l-valyl-l-leucine. *Acta Crystallogr. C* **1990**, *C46*, 243-246.
(54) Ramachandran, R.; Lewandowski, J. R.; van der Wel, P. C. A.; Griffin, R. G. Multipole-multimode Floquet theory of rotational resonance width experiments: C13–C13 distance measurements in uniformly labeled solids. *J. Chem. Phys.* **2006**, *124*, 214107.
(55) Mueller, L.; Ernst, R. R. Coherence transfer in the rotating frame - application to heteronuclear cross correlation spectroscopy. *Mol. Phys.* **1979**, *38*, 963-992.

(56) Can, T. V.; Ni, Q. Z.; Griffin, R. G. Mechanisms of dynamic nuclear polarization in insulating solids. *J. Magn. Reson.* **2015**, *253*, 23–35.
(57) Wang, T.; Williams, J.; Schmidt-Rohr, K.; Hong, M. Relaxation-compensated difference spin diffusion NMR for detecting ^{13}C–^{13}C long-range correlations in proteins and polysaccharides. *J. Biomol. NMR* **2015**, *61*, 97-107.
(58) Frantsuzov, I.; Ernst, M.; Brown, S. P.; Hodgkinson, P. Simulating spin dynamics in organic solids under heteronuclear decoupling. *Solid State Nucl. Magn. Reson.* **2015**, *70*, 28-37.
(59) Veshtort, M.; Griffin, R. G. SPINEVOLUTION: A powerful tool for the simulation of solid and liquid state NMR experiments. *J. Magn. Reson.* **2006**, *178*, 248-282.
(60) Hogben, H. J.; Krzystyniak, M.; Charnock, G. T. P.; Hore, P. J.; Kuprov, I. Spinach – A software library for simulation of spin dynamics in large spin systems. *J. Magn. Reson.* **2011**, *208*, 179-194.
(61) Veshtort, M.; Griffin, R. G. High-performance selective excitation pulses for solid- and liquid-state NMR spectroscopy. *ChemPhysChem* **2004**, *5*, 834-850.

TOC Graphic

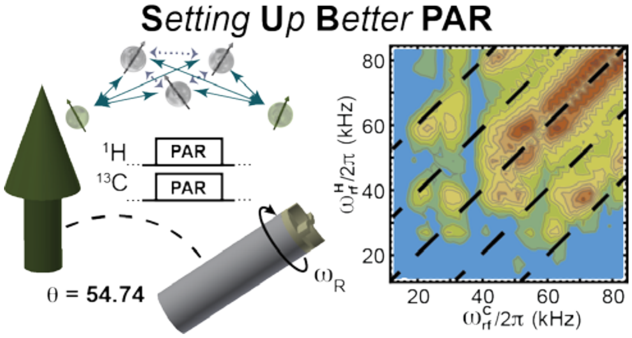
Setting Up Better PAR
1H
13C
PAR
PAR
θ = 54.74
ωR
80
60
40
20
ω rf H/2π (kHz)
20
40
60
80
ω rf C/2π (kHz)